Effect of annealing and applied bias on barrier shape in CoFe/MgO/CoFe tunnel junctions

Yuzi Liu,[1,*] Ann N. Chiaramonti,[1] Daniel K. Schreiber,[1,2] Hyunsoo Yang,[3] Stuart S. P. Parkin,[4]
Olle G. Heinonen,[1] and Amanda K. Petford-Long[1,5]

[1] *Materials Science Division, Argonne National Laboratory, Argonne, Illinois 60439, USA*
[2] *Department of Materials Science and Engineering, Northwestern University, Evanston, Illinois 60208, USA*
[3] *Department of Electrical and Computer Engineering, National University of Singapore, Singapore 117576, Singapore*
[4] *IBM Almaden Research Center, 650 Harry Road, San Jose, California 95120, USA*
[5] *Center for Nanoscale Materials, Argonne National Laboratory, Argonne, Illinois 60439, USA*

(Received 26 August 2010; revised manuscript received 23 February 2011; published 12 April 2011)

Energy-filtered transmission electron microscopy and electron holography were used to study changes in the MgO tunnel barrier of CoFe/MgO/CoFe magnetic tunnel junctions (MTJs) as a function of annealing and *in situ* applied electrical bias. Annealing was found to increase the homogeneity and crystallinity of the MgO tunnel barrier. Cobalt, oxygen, and trace amounts of iron diffused into the MgO upon annealing. Annealing also resulted in a reduction of the tunneling barrier height, and decreased the resistance of the annealed MTJ relative to that of the as-grown sample. *In situ* off-axis electron holography was employed to image the barrier potential profile of a MTJ directly, with the specimen under electrical bias. Varying the bias voltage from −1.5 to +1.5 V was found to change the asymmetry of the barrier potential and decrease the effective barrier width as a result of charge accumulation at the MgO-CoFe interface.

DOI: 10.1103/PhysRevB.83.165413 PACS number(s): 61.05.jp, 81.40.Ef, 73.40.Gk, 68.37.Lp

I. INTRODUCTION

Metal-oxide interfaces are the subject of extensive experimental and theoretical research for next generation nanoscale spintronic devices that exploit spin as a degree of freedom for charged electrons.[1] They play a key role in metal-oxide based science and engineering, with applications including magnetic tunnel junctions (MTJs)[2] and other heterogeneous structures such as resistance switching oxides[3] with uses or potential uses in low-power nonvolatile memories. In its simplest form, the MTJ is a trilayer structure consisting of two ferromagnetic (FM) electrode layers separated by an ultrathin dielectric layer. The electrical resistance across the insulating tunnel barrier is dependent upon the relative orientation of the magnetizations of the two ferromagnetic electrodes. In most cases, the electrical resistance is lower when the magnetization of the two ferromagnetic layers is parallel and higher when the magnetization is antiparallel.[4] This difference in resistance between the two magnetization configurations is quantified by the tunneling magnetoresistance (TMR). MTJs have attracted the attention of experimental and theoretical scientists for their application as magnetic-field sensors in hard disk drives and as the memory element in nonvolatile magnetic random access memories (MRAM).[5] MTJs with crystalline tunnel barriers such as MgO are of particular interest as they have been theoretically predicted[6] and experimentally verified[7,8] to exhibit extremely high values of TMR, which is required for device applications, as a result of an enhanced tunneling spin polarization from the spin-filter effect.

It is well known that the barrier layer plays a critical role in the transport behavior of MTJs. For example, MTJs in which single-crystal MgO is substituted for amorphous AlO_x in the tunnel barrier showed greatly enhanced TMR[6–8] as a result of the coherent tunneling of electrons through the barrier. The barrier shape is sensitive to many factors. An asymmetric barrier can be induced by effects such as differences in the crystal structure of the two FM layers on either side of it,[9] the degree of oxidation of the tunnel barrier,[10] and intermixing of elements at the barrier interfaces after annealing.[11] The most straightforward method of tuning the barrier asymmetry is by applying a bias voltage.[12] The conductance of the MTJ is another important parameter that must be considered for its use in hard drive disk read head applications, and careful processing of MgO-based MTJs has led to resistance-area products as low as 0.4 $\Omega\ \mu m^2$ with 50% TMR.[13]

In general, the transport properties of MTJs depend on many factors, such as band-structure effects[14] and spin scattering.[15] Microstructural changes have been used to explain the transport behavior of MTJs after various postdeposition treatments.[16–18] In particular, vacuum annealing has been observed to increase the TMR of MTJs with crystalline MgO barrier layers.[19,20] This increase in TMR can be associated with an increased tunneling spin polarization (SP),[8] a more uniform barrier layer,[21] and/or lower roughness and less interdiffusion at the interfaces between the tunnel barrier and the ferromagnetic electrodes.[22–24] It has been reported that the conductance of the parallel magnetization configuration increases after annealing.[25] On the other hand, there are also reports that the resistance-area product does not change during postdeposition annealing[26] or increases with annealing temperature.[27] The asymmetry in the shape of the barrier potential has been probed by using photoconductance[10] and off-axis electron holography,[23,28] which allowed the asymmetric voltage dependence of the electron transport behavior to be observed.

Transmission electron microscopy (TEM) is a powerful tool in the study of the microstructure and chemical distribution of materials at the subnanometer scale, and has proven to be particularly useful in the study of MTJs.[23,29–32] High-resolution TEM (HREM) has been applied to study the Fe/MgO interface in epitaxial MTJs[31] and microstructure evolution in MTJs following annealing.[33] The interfacial roughness of Fe/MgO/Fe MTJs[34] and the segregation of B and

 ©2011 American Physical Society

O at the CoFeB/MgO interfaces in polycrystalline Mg-B-O (Ref. 35) have been measured by a combination of electron energy loss spectroscopy (EELS) and scanning TEM (STEM) on the atomic scale. Recently, *in situ*, site-specific electrical biasing TEM experiments were introduced,[36] allowing direct correlation between the microstructure and transport behavior.[37,38] The chemical composition of the tunnel barrier and its interfaces with the electrodes is a controlling factor in the spin-dependent tunneling effect needed for high TMR. However, the exact evolution of the barrier shape as a function of changes to the barrier composition and structure during annealing is still not well understood, and the way in which barrier potential symmetry and effective width vary as a function of an applied electrical bias is also not fully understood.

We have used HREM, energy-filtered TEM (EFTEM), and *in situ* electron holography under an applied bias to study the MgO tunnel barrier of a CoFe/MgO/CoFe MTJ with the goal of understanding the barrier shape evolution as a function of annealing and electrical bias. HREM was used to reveal the crystalline quality of the MgO and its interfaces with CoFe before and after annealing. The tunneling behavior of the as-grown and annealed samples was determined by site-specific measurements of the current density-voltage (J-V) characteristics. The evolution of the elemental distributions of Co, Fe, and O upon annealing was also studied in detail by EFTEM. Finally, *in situ* off-axis electron holography was used to probe the potential barrier shape, asymmetry, and effective width in both unbiased and biased conditions.

II. EXPERIMENTAL DETAILS

The multilayer MTJ structure was deposited on a high-conductivity Si(100) substrate ($\rho < 0.001\ \Omega$ cm) after removing the native oxide with HF etching with the following stack sequence: Si/TaN(10)/Ta(5)/IrMn(25)/$Co_{49}Fe_{21}B_{30}$(0.3)/$Co_{70}Fe_{30}$(3.5)/MgO(3.6)/$Co_{70}Fe_{30}$(2)/$Co_{49}Fe_{21}B_{30}$(10)/Ta(7.5)/TaN(7.5)/Cr(60), where the numbers in parentheses denote the layer thickness in nanometers. The metallic layers were deposited by dc magnetron sputtering in 3 mTorr Ar. The MgO barrier layer was deposited by reactive deposition of a metallic Mg target in an Ar-O_2 mixture. One piece of the Si wafer was annealed at 300 °C in high vacuum for 30 min. The samples for standard cross-sectional TEM imaging were prepared by a focused-ion beam (FIB) lift-out technique.[39] Samples for *in situ* electron holography experiments were prepared as described elsewhere.[36] Off-axis electron holography requires that the area of interest (in this case, the MgO barrier) must be close to the vacuum edge of the sample (several tens of nanometers, maximum). In order to meet this requirement, the sample was imaged (lightly etched) with a 5-kV Ga^+ ion beam in the FIB until the MgO was very near the exposed surface. The 5-kV Ga^+ damage at the surface may also introduce some additional contact resistance, which is expected to be small in comparison to the resistance of the relatively thick MgO tunnel barrier layer in these particular samples, and will therefore be neglected.[36,37] All analytical TEM experiments were carried on a FEI Tecnai F20 TEM. Site-specific current-voltage (I-V) transport characteristics were measured in an electrical biasing stage inside of the TEM with the bottom electrodes grounded, as described in detail elsewhere.[36] A pseudo four-point probe dc method in voltage sourcing mode was used. A gold tip (50-nm end radius) was positioned to touch the specimen surface using piezoelectric motors, which can be controlled in three dimensions with nanometer accuracy.[36] The gold probe tip was in constant contact with the specimen during data collection (i.e., the contact area between the Au probe and sample was constant throughout each I-V curve measurement), and the tip morphology was carefully preserved throughout the series of experiments in order to minimize the variations in the contact resistance. The *in situ* applied bias voltage was set manually in increments of 0.25 V from -1.5 to $+1.5$ V. In order to obtain good statistics and smooth the I-V curves, the applied voltage was held for 5 s at every step and each reported data point for a given voltage is the average of $\sim$100 individual current measurements recorded during the 5 s interval. Note that all electrical measurements were made in the parallel magnetization configuration of the two ferromagnetic electrodes (low resistance state). The tunneling current measured from the I-V characteristic was normalized to the electrode contact area to yield the current density (J), which is used as the fitting parameter for data analysis. The local effective barrier height and width values were extracted from the experimental transport data by fitting to the Brinkman-Dynes-Rowell (BDR) model[40] for tunneling through the insulating barrier. The three-window background subtraction[41] method for EFTEM was applied to obtain the elemental distributions of Co, Fe, and O. A biprism biased at +160 V was used for the off-axis electron holography. The reconstructed phase-shift profile was used to measure the electrostatic potential of the tunnel barrier and thus directly probe the barrier shape and determine the effective barrier layer width. Here, the phase shift of the electron beam can be simply written as[42]

$$\varphi = C_E \phi t, \tag{1}$$

where $C_E = 7.3 \times 10^{-3}$ rad V^{-1} nm^{-1} for 200 kV electrons, ϕ is the electrostatic potential, and $\phi = V_0$ (V_0 is the mean inner potential) when there is no external electric field applied. This equation can also be applied to map the chemical homogeneity if the sample thickness (t) is constant[23] within the area of interest. The holography data were processed by reconstruction with reference images using the Holoworks[43] data processing software for Digital Micrograph™. The electron phase shift is plotted with a 200-pixel-wide line scan from the phase-shift image. The phase-shift curves were fitted using Gaussian functions at the CoFe/MgO interfaces and a linear fit that connected the two Gaussians across the barrier. The effective barrier width was measured as the sum of half the width of the Gaussian at each interface plus the distance between the peaks of the Gaussians.

III. RESULTS AND DISCUSSION I: EFFECTS OF ANNEALING

A low-magnification bright-field TEM image of the as-grown sample is shown in Fig. 1(a). The growth direction is from the bottom to the top of the image. The mass-thickness

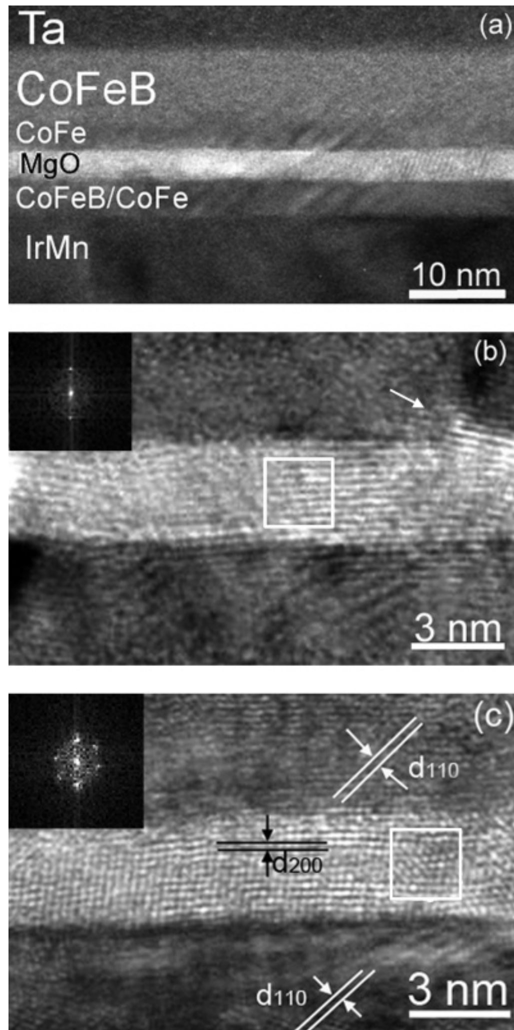

FIG. 1. (a) Low-magnification TEM image of the MgO-based MTJ device multilayer structure. HREM images close to the barrier area of (b) as-grown and (c) annealed samples. The FTs of MgO layer are shown as insets in (b) and (c).

contrast in the image clearly highlights the multilayer structure of the sample. The MgO layer shows the brightest contrast because of its low average atomic number. It is difficult to distinguish the ultrathin 0.3-nm-thick CoFeB layer from the 3.5-nm-thick CoFe layer below the MgO barrier layer. The top CoFeB layer can, however, be distinguished from the CoFe layer just above the barrier due to its amorphous nature arising from its high B content. HREM images near the MgO barrier of the as-grown and annealed specimens are shown in Figs. 1(b) and 1(c), respectively. In the as-grown sample the top electrode is amorphous and the CoFe-on-MgO interface is rougher than the MgO-on-CoFe interface. An area in the rough interface where the MgO protrudes into the top CoFe layer is marked with the white arrow in Fig. 1(b). There are some crystalline lattice fringes observed in the MgO, which means the MgO was at least partially crystalline in the as-grown sample. After annealing, the two CoFe ferromagnetic layers show a highly oriented [100] out-of-plane texture, as does the MgO barrier layer, as seen in Fig. 1(c). Following annealing, the amorphous CoFeB layers in the as-grown sample were crystallized by exclusion of B to form CoFe, which is consistent with previous research.[44,45] By comparing the as-grown and annealed structures in Figs. 1(b) and 1(c) and the digital Fourier transforms (FTs) of the MgO layer (insets), it can be seen that the crystallinity of both the MgO and CoFe layers has greatly improved after annealing. Sampling from a larger cross-sectional area also showed that the CoFe-on-MgO interfacial roughness has reduced after annealing. To quantify this effect, the rms interfacial roughness of the MgO-on-CoFe and CoFe-on-MgO interfaces, shown in Table I, were measured directly via three-dimensional electron tomography.[46] As can be seen from the values in Table I, the measured roughness of the MgO-on-CoFe interface is smaller than that of the CoFe-on-MgO interface in the as-grown sample. The roughness of the CoFe-on-MgO interface was reduced from 0.20 ± 0.02 to 0.12 ± 0.01 nm by annealing. In contrast, the roughness of the bottom MgO interface was unchanged after annealing.

TABLE I. The interface roughness extracted from STEM tomography.

	CoFe-on-MgO (nm)	MgO-on-CoFe (nm)
As-grown	0.20 ± 0.02	0.138 ± 0.004
Annealed	0.12 ± 0.01	0.135 ± 0.007

The sample for *in situ* site-specific *I-V* experiments was patterned using the FIB to form many horizontal pillars varying in size from 500 nm to 1 μm in width, as seen in Fig. 2(a). Figure 2(b) shows a representative image of the Au probe contacted to the top of a 1-μm-diam pillar. Note that the sample is thin (<100 nm thickness) in the direction of the electron beam in order to enable TEM observation. Annealing resulted in a major change in the transport behavior of the tunnel junction. The resulting experimental *J-V* curves are shown in Fig. 3, where J is the current density in A/cm^2, and V is the bias voltage in volts. Both samples show tunneling *J-V* characteristics but with some obvious differences. Most significantly, the current density of the annealed sample (22 A/cm^2) under an applied bias voltage of 0.75 V is much higher than that of the as-grown sample (12 A/cm^2) at the same bias. Least-squares regression fitting of the *J-V* curves

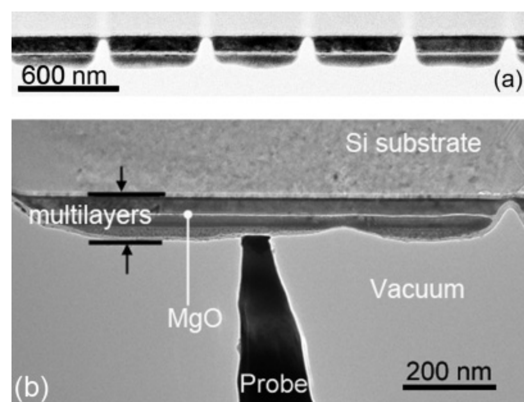

FIG. 2. (a) TEM image of an *in situ* sample with five separate pillars. (b) TEM image showing the morphology of one pillar in contact with the Au probe during *I-V* measurement.

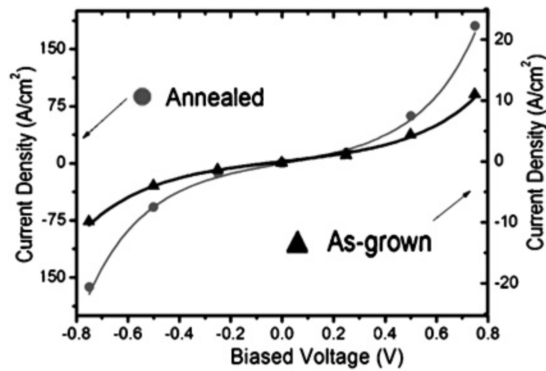

FIG. 3. Plots of current density versus voltage for the as-grown and annealed samples.

to the BDR model[40] through an asymmetric tunnel barrier yielded a decrease in the estimated barrier height from 1.14 to 0.50 eV, while the estimated barrier width increased from 1.9 nm as-grown to 2.6 nm annealed as shown in Table II.

Figure 4(a) shows the standard reconstructed electron wave phase-shift image of the as-grown sample as measured by off-axis electron holography. The dark areas correspond to the top and bottom CoFe electrodes. The bright area across the center of the image is the MgO barrier layer. From the large difference in contrast between the MgO and the CoFe electrodes, we can conclude that there is a significant difference in the phase shift of the electron beam in these areas. A line scan of the electron phase shift across the tunnel junction is shown in Fig. 4(b). The phase shift is normalized to the sample thickness in the region of the FM electrodes in order to plot the relative phase shift in the MgO barrier layer of both samples. The phase shift of the barrier layer in the annealed sample is lower than that of the as-grown sample. The measured barrier layer width (t_{phase}) in the annealed sample is 3.2 ± 0.1 nm, which is larger than the 2.8 ± 0.1 nm barrier width of the as-grown sample. This implies that after annealing, the effective barrier layer width has expanded slightly. We note that the small phase-shift oscillations across the MgO barrier area most likely arise from a combination of lattice fringes, hologram interference fringes, and Fresnel fringes at the edges of the biprism.[47]

EFTEM imaging was used to map the elemental distribution of Co, Fe, and O in the MTJ, in an attempt to explain the higher current density and the smaller phase shift in the annealed sample as observed in the *J*-*V* measurements (Fig. 3) and the electron holography data [Fig. 4(b)]. Figure 5(a) shows superimposed the color-coded Co (red), Fe (green), and O (blue) elemental distributions of the annealed sample. The MgO barrier area tracks with the presence of oxygen

TABLE II. Barrier parameters from BDR fitting and phase shift.

		As-grown	Annealed
BDR fitting	Height (eV)	1.14	0.5
	Width (nm)	1.9	2.6
Phase shift	Phase-shift height (rad)	3.43 ± 0.03	3.27 ± 0.03
	Width (nm)	2.8 ± 0.1	3.2 ± 0.1

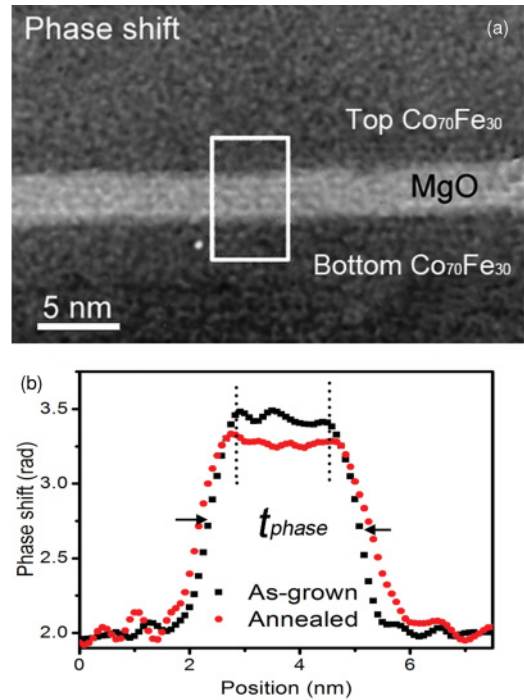

FIG. 4. (Color online) (a) Phase-shift image of the as-grown MTJ reconstructed from the hologram. (b) Line scan of the phase-shift profile averaged over 200 pixels parallel to the barrier layer. Profile corresponds to the boxed region in (a).

and therefore is predominantly blue. In order to display the elemental distribution more clearly, 50-pixel-wide line scans [perpendicular to the barrier, as the white profile marked in Fig. 5(a)] of the elemental intensities are plotted in Figs. 5(b)–5(d) for Co, Fe, and O, respectively. The counts (arbitrary units) of the Co and Fe distribution profiles are normalized to that of the bottom CoFe electrode in the as-grown and annealed samples. A larger number of counts (higher intensity) indicates a higher relative elemental concentration. In order to compare the elemental distributions quantitatively, the average barrier width $\langle t_{\text{element}} \rangle$ was determined from the Co, Fe, and O elemental distributions by averaging t_{element} (t_{element} was determined as the distance between the points where the counts have reached 50% of the difference between the minimum and maximum values on either side of the barrier) from the line profiles shown in Figs. 5(b)–5(d) at five different locations. $\langle t_{\text{element}} \rangle$ for the annealed and as-grown samples, for both the Co and the Fe distributions, agree within experimental uncertainty. However, by comparing the data points in the center of the MgO layer between the two vertical dashed lines in both Figs. 5(b) and 5(c), it can be seen that a significant amount of Co appears to have diffused into the tunnel barrier during annealing, along with a small amount of Fe, as indicated by the higher normalized counts in the annealed sample. While it is not possible to measure accurately the absolute concentration of Co within the barrier from these data,[48] it is possible to make a comparison between the as-grown and annealed samples, and thus to see that there is an increase of ~7% in Co concentration in the barrier area after annealing. This was determined by normalizing the Co counts to the nominal Co content in the lower FM electrode. In terms of the

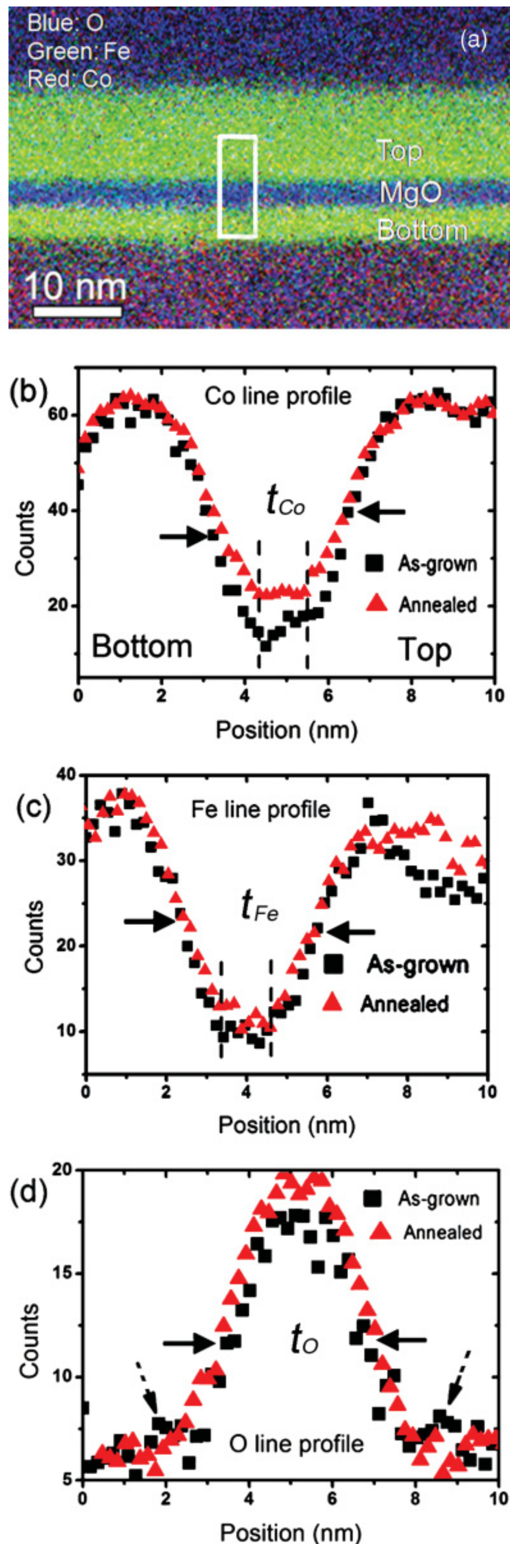

FIG. 5. (Color online) (a) Composite elemental of O (blue), Fe (green), and Co (red) obtained from EFTEM data; normalized intensity profiles for (b) Co, (c) Fe, and (d) O.

oxygen distribution before annealing, small peaks are present on either side of the main oxygen peak in the as-grown sample, indicated by dashed arrows in Fig. 5(d), which correspond to a higher O content at the MgO/CoFe interfaces. These small peaks disappear after annealing. In addition, $\langle t_O \rangle$ increases from 2.9 ± 0.1 to 3.4 ± 0.1 nm upon annealing. Previous work using x-ray photoelectron spectroscopy (XPS) showed that annealing results in substantial Fe and Co diffusion into the MgO barrier in a simple Ta/CoFe/MgO/Ru stack.[49] Here, EFTEM revealed Co, Fe, and O interdiffusion between the barrier and electrodes after annealing, which induces the apparent increase in barrier width. The fact that more Co diffused into the MgO than Fe is attributed to the much higher Co concentration of the FM layers in the as-deposited sample.

Although the composition profiles can be used to estimate the width of the tunnel barrier, the barrier width estimated from t_{phase} is the easiest to understand in that it differentiates between regions of low average atomic number, namely, oxide that might be expected to form part of the tunnel barrier, and the metal electrodes on either side. The increase in barrier width after annealing as measured by electron holography (t_{phase}) agrees qualitatively with the BDR model fitting results. However, the barrier width obtained by BDR fitting to the *J-V* data is smaller than that measured from the phase images for both the as-grown and annealed samples. This is not surprising. First, the BDR model is based on a free-electron mass and free-electron dispersion relation, while a crystalline CoFe/MgO/CoFe MTJ has a different dispersion relation (and effective mass) in the majority band (Δ_1). This would lead to a difference in barrier width as compared with the simple BDR model, even for perfect crystalline junctions. For the MTJs analyzed in this study, the crystallinity is not perfect, Co and Fe have diffused into the barrier, and the barrier width is not uniform. The parameters extracted from the BDR model are known to be sensitive to defects[50] and non-ideal (e.g., rough) barrier-electrode interfaces. Additionally, tunneling occurs preferentially through the thinnest parts of the barrier, even if it is localized to the small area under the probe tip. All these effects would induce the smaller barrier width obtained by BDR fitting to the *in situ J-V* measurements.

From the *in situ J-V* measurements it is clear that the MTJ resistance decreases during annealing. The annealing time and annealing temperature are both critical to the conductance and TMR of MTJs. The EFTEM data presented here show that annealing leads to chemical reduction of the oxidized CoFe electrode regions at the CoFe/MgO interfaces in the as-grown sample, and to oxygen being driven into the barrier layer.[51,52] Diffusion of O into the MgO would reduce the density of O vacancies within the barrier and probably results in a more stoichiometric MgO composition. In contrast, Co and Fe are impurities in the MgO tunnel barrier which act as tunneling mediators[53] and may even form conducting channels[54] that reduce the effective barrier height, resulting in lower barrier resistance. Even if the Co and Fe atoms are oxidized within the MgO layer, since the band gaps of CoO (3 eV) (Refs. 55 and 56) and FeO (2.5 eV) (Refs. 56 and 57) are much smaller than the band gap of MgO (7.7 eV),[58,59] the formation of mixed oxide phases will again reduce the barrier height. Finally, the crystallinity of the top and bottom CoFe electrodes was improved by annealing. Thus, the lower parallel resistance after annealing may in part be attributed to better crystallinity and lattice matching of the electrodes with the MgO barrier layer.[25,60]

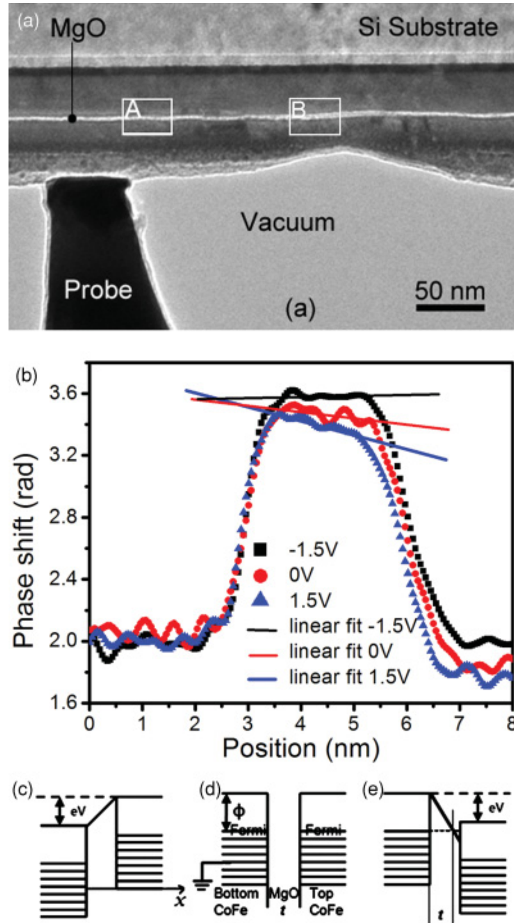

FIG. 6. (Color online) (a) Low-magnification TEM image of the areas used for *in situ* biased electron holography experiments. (b) Line scan of the phase-shift profile averaged over 200 pixels parallel to the barrier layer for different applied bias voltages of −1.5, 0, and +1.5 V taken from region A. The lower panel shows a schematic illustrating the barrier potential shape under (c) negative bias, (d) zero bias, and (e) positive bias.

IV. RESULTS AND DISCUSSION II: BIASING EFFECTS

The results presented above have shown that annealing changes the barrier shape by reducing the effective barrier height and increasing the effective barrier width. It is, however, also interesting to consider the effects of the biasing voltage itself on the tunnel barrier potential shape. To do this, the as-grown MTJ was biased *in situ* in the TEM and characterized by a combination of *I-V* measurement and electron holography in the area marked "A" in Fig. 6(a). The holograms were taken with the sample under differing bias voltages. The bottom ferromagnetic electrode was grounded during the measurements. Under the biased condition, the electrostatic potential $\phi(x)$ in Eq. (1) can be rewritten as

$$\phi(x) = V_0 - Ex, \tag{2}$$

where E is the simplified equivalent electric-field strength in the tunnel barrier area when the barrier layer is biased and the MTJ acts as a capacitor.[61] V_0 (mean inner potential) is a constant and x is the distance across the barrier as shown

TABLE III. The slopes of the electron phase shift from phase-shift curves.

	Under contact (nm^{-1})	Away from contact (nm^{-1})
−1.5 V	∼0	−0.03
0 V	−0.04	−0.04
1.5 V	−0.09	−0.04

in Fig. 6(c). The sample bias was kept below 1.5 V to avoid dielectric breakdown.

Phase-shift plots were obtained for three bias voltages (−1.5, 0, and +1.5 V) and are shown in Fig. 6(b). The linear fit to the phase-shift plots inside the barrier area recorded at bias values of −1.5, 0, and 1.5 V yields slopes of∼0, −0.04, and −0.09 nm^{-1}, respectively, as shown in Table III. Each value is the average of three measurements made in the region in which the probe contacts with the surface of the sample and the experimental uncertainty is ±0.01 nm^{-1}. Note that the shape of the barrier in the unbiased condition is still a trapezoid, indicating that the MgO barrier itself is asymmetric even prior to electrical biasing. The mean inner potential (V_0) contribution to the phase shift is constant under the different biased conditions. Therefore, the difference observed in the slope of the three phase-shift plots is a direct result of the applied electrical bias, which can be explained using Eq. (2) by considering the change in electric-field direction as the voltage is changed from positive to negative. The average barrier width changes by ∼0.2 nm between the +1.5 V bias case and the unbiased case, and between the unbiased case and a bias of −1.5 V.

The potential landscape in the barrier layer of a MTJ is important in helping to understand the transport properties.[40,62] The barrier potential asymmetry can be strongly modified by the presence of an inhomogeneous or composite barrier layer[23,63] and/or an electric field, for example, as a result of dissimilar work functions if the two electrodes are composed of different materials.[64] The tuning of the barrier asymmetry as a function of applied voltage is illustrated schematically in Figs. 6(c)–6(e). Here the left electrode, which corresponds to the bottom electrode in the sample growth direction, is grounded. When negative bias voltage is applied [Fig. 6(c)], the right-hand side of the barrier is pushed up to form a trapezoid-shaped barrier potential. In contrast, when a positive bias voltage was applied [Fig. 6(e)], the trapezoid shape is reversed as compared to the negative bias voltage of Fig. 6(c). In general, under a biased condition, charge will build up at the interfaces between the metal-insulator-metal junction and lead to the well-known electron screening effect, causing electric-field penetration into the metal.[65,66] In our experiments, a negative bias voltage will increase the barrier height at the top interface as shown in Fig. 6(c) and will cause more electrons to accumulate near the interface, thus increasing the effective barrier width. However, when the bias voltage is positive, the barrier height will be lowered at the top interface, and for the case when the applied voltage is greater than the unbiased barrier height, the effective barrier width will be decreased.[12] The holography data suggest that the bias voltage not only regulates the barrier symmetry but also affects

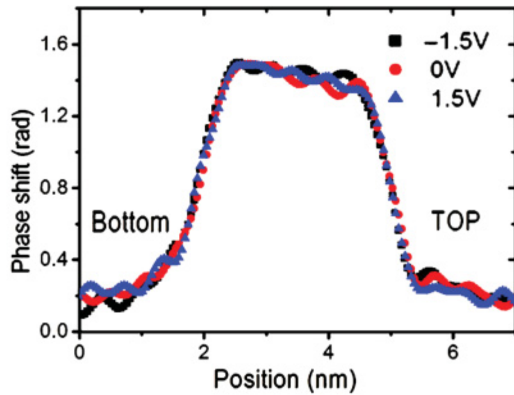

FIG. 7. (Color online) The averaged phase-shift profile under different biased voltages of −1.5, 0, and +1.5 V taken from region B of Fig. 6(a).

the effective barrier width. The dependence of effective barrier width on the bias voltage needs further theoretical study.

The slopes of the phase shift near the interfaces of the barrier layer obtained during the *in situ* biasing experiment [Fig. 6(b)] are not as sharp as they are in Fig. 4(b), which was obtained from a standard cross-section sample. In addition, t_{phase} for the unbiased case (3.03 ± 0.02 nm), measured on the *in situ* biasing sample, is larger than that of the as-grown standard cross-section sample (2.80 ± 0.09 nm). First, it should be remembered that these are measurements made on two different samples, as standard cross-section samples are not suitable for *in situ* biasing experiments. Second, and more significantly, this is due to the practical tilt limitations of the *in situ* biasing holder. For the standard cross-section sample [Fig. 4(b)] a double-tilt holder was used which allowed the interfaces to be aligned parallel with the electron beam. The *in situ* TEM holder, in contrast, has an internal tilt mechanism that only allows the sample to be tilted within 1°–2°of a zone axis reliably and reproducibly. Thus the interfaces in the *in situ* sample were not as close to the parallel imaging configuration as for the standard cross-section sample, resulting in the layers partially overlapping in projection, which would reduce the apparent projected interface sharpness in the phase-shift curves and broaden the measured width.

In order to assess the lateral current spreading in the FM electrodes, the same *in situ* biasing electron holography experiment was performed at the position marked "B" in Fig. 6(a), which is ∼150 nm away from the probe-sample contact position. The phase-shift results using the same data process method as Fig. 6(b) are shown in Fig. 7. In each case the values shown are the average of seven measurements made at points away from the contact to the sample. The averaged values of the slopes close to and away from the contact are shown in Table III. In contrast to the measurements carried out under the probe contact, the measurements carried out away from the contacts show no change in either slope or effective barrier width with respect to applied bias, within experimental uncertainty. This implies that the effect of the biasing potential is localized to within less than 150 nm on either side of the probe contact area and further confirms that the *J-V* curve measured in the pseudo-four-point *in situ* holder is site specific. This is believed to occur because of a very thin oxide layer at the top surface of the specimen which leads to ballistic transport across the tunnel barrier.[36] Similar localization effects were observed by Wulfhekel *et al.*[67] as lateral variations in the conductance in Fe/MgO/Fe MTJs using atom force microscopy (AFM) in contact mode.

V. CONCLUSIONS

In summary, the tunneling barrier evolution in an MgO-based magnetic tunnel junction as a function of annealing and externally applied bias was studied using EFTEM and *in situ* electron holography. Co and Fe diffusion into the MgO layer after annealing led to a reduction in tunnel barrier height. In addition, the oxidized CoFe/MgO interfaces were reduced by annealing and the O was absorbed by the MgO layer. Improved crystallinity of the MgO barrier and crystallization of the CoFeB layers were also observed after annealing. The change in effective MgO tunnel barrier width and asymmetry as a function of annealing and applied bias were probed using *in situ* electron holography. The change in barrier width under applied bias can be explained by charge accumulation at the interface between the MgO tunnel barrier and CoFe ferromagnetic electrodes. The localization of the electric transport measurements in our *in situ* experiments is confirmed by electron holography.

ACKNOWLEDGMENTS

The authors thank Kenneth D'Aquila for help in fitting the phase-shift curves. Argonne National Laboratory is operated under Contract No. DE-AC02-06CH11357 by the US DOE. The electron microscopy was accomplished in the Argonne National Laboratory Electron Microscopy Center for Materials Research.

*yuziliu@anl.gov

[1]S. A. Wolf, D. D. Awschalom, R. A. Buhrman, J. M. Daughton, S. von Molnar, M. L. Roukes, A. Y. Chtchelkanova, and D. M. Treger, Science **294**, 1488 (2001).
[2]II Oleynik and E. Y. Tsymbal, Interface Sci. **12**, 105 (2004).
[3]S. Tsui, A. Baikalov, J. Cmaidalka, Y. Y. Sun, Y. Q. Wang, Y. Y. Yue, C. W. Chu, L. Chen, and A. J. Jacobson, Appl. Phys. Lett. **85**, 317 (2004).
[4]M. Julliere, Phys. Lett. A **54**, 225 (1975).
[5]S. S. P. Parkin, K. P. Roche, M. G. Samant, P. M. Rice, R. B. Beyers, R. E. Scheuerlein, E. J. O'Sullivan, S. L. Brown, J. Bucchigano, D. W. Abraham, Y. Lu, M. Rooks, P. L. Trouilloud, R. A. Wanner, and W. J. Gallagher, J. Appl. Phys. **85**, 5828 (1999).
[6]W. H. Butler, X. G. Zhang, T. C. Schulthess, and J. M. MacLaren, Phys. Rev. B **63**, 054416 (2001).

[7] S. Yuasa, T. Nagahama, A. Fukushima, Y. Suzuki, and K. Ando, Nat. Mater. **3**, 868 (2004).
[8] S. S. Parkin, C. Kaiser, A. Panchula, P. M. Rice, B. Hughes, M. Samant, and S.-H. Yang, Nat. Mater. **3**, 862 (2004).
[9] P. LeClair, J. T. Kohlhepp, C. H. van de Vin, H. Wieldraaijer, H. J. M. Swagten, W. J. M. de Jonge, A. H. Davis, J. M. MacLaren, J. S. Moodera, and R. Jansen, Phys. Rev. Lett. **88**, 107201 (2002).
[10] P. H. P. Koller, H. J. M. Swagten, W. J. M. de Jonge, H. Boeve, and R. Coehoorn, Appl. Phys. Lett. **84**, 4929 (2004).
[11] H. Bruckl, J. Schmalhorst, G. Reiss, G. Gieres, and J. Wecker, Appl. Phys. Lett. **78**, 1113 (2001).
[12] J. G. Simmons, J. Appl. Phys. **34**, 1793 (1963).
[13] Y. Nagamine, H. Maehara, K. Tsunekawa, D. D. Djayaprawira, N. Watanabe, S. Yuasa, and K. Ando, Appl. Phys. Lett. **89**, 162507 (2006).
[14] A. M. Bratkovsky, Phys. Rev. B **56**, 2344 (1997).
[15] F. Guinea, Phys. Rev. B **58**, 9212 (1998).
[16] T. Takeuchi, K. Tsunekawa, Y. S. Choi, Y. Nagamine, D. D. Djayaprawira, A. Genseki, Y. Hoshi, and Y. Kitamoto, Jpn. J. Appl. Phys., Part 2 **46**, L623 (2007).
[17] J. H. Lee, H. D. Jeong, H. Kyung, C. S. Yoon, C. K. Kim, B. G. Park, and T. D. Lee, J. Appl. Phys. **91**, 217 (2002).
[18] K. I. Lee, J. H. Lee, W. Y. Lee, K. W. Rhie, J. G. Ha, C. S. Kim, and K. H. Shin, J. Magn. Magn. Mater. **239**, 120 (2002).
[19] J. Hayakawa, S. Ikeda, Y. M. Lee, F. Matsukura, and H. Ohno, Appl. Phys. Lett. **89**, 232510 (2006).
[20] R. Wang, X. Jiang, R. M. Shelby, R. M. Macfarlane, S. S. P. Parkin, S. R. Bank, and J. S. Harris, Appl. Phys. Lett. **86**, 052901 (2005).
[21] S. Cardoso, P. P. Freitas, Z. G. Zhang, P. Wei, N. Barradas, and J. C. Soares, J. Appl. Phys. **89**, 6650 (2001).
[22] M. Yamamoto, T. Marukame, T. Ishikawa, K. Matsuda, T. Uemura, and M. Arita, J. Phys. D **39**, 824 (2006).
[23] Y.-Z. Liu, W. G. Wang, T. Moriyama, J. Q. Xiao, and Z. Zhang, Phys. Rev. B **75**, 134420 (2007).
[24] J. M. De Teresa, A. Barthelemy, A. Fert, J. P. Contour, R. Lyonnet, F. Montaigne, P. Seneor, and A. Vaures, Phys. Rev. Lett. **82**, 4288 (1999).
[25] W. G. Wang, C. Ni, G. X. Miao, C. Weiland, L. R. Shah, X. Fan, P. Parson, J. Jordan-sweet, X. M. Kou, Y. P. Zhang, R. Stearrett, E. R. Nowak, R. Opila, J. S. Moodera, and J. Q. Xiao, Phys. Rev. B **81**, 144406 (2010).
[26] S. Isogami, M. Tsunoda, K. Komagaki, K. Sunaga, Y. Uehara, M. Sato, T. Miyajima, and M. Takahashi, Appl. Phys. Lett. **93**, 192109 (2008).
[27] T. Dimopoulos, G. Gieres, J. Wecker, N. Wiese, Y. Luo, and K. Samwer, J. Appl. Phys. **98**, 073705 (2005).
[28] F. Shen, T. Zhu, X. H. Xiang, J. Q. Xiao, E. Voelkl, and Z. Zhang, Appl. Phys. Lett. **83**, 5482 (2003).
[29] A. K. Petford-Long and A. N. Chiaramonti, Annu. Rev. Mater. Res. **38**, 559 (2008).
[30] A. K. Petford-Long, A. Kohn, T. Bromwich, V. Jackson, F. Castano, and L. J. Singh, Thin Solid Films **505**, 10 (2006).
[31] C. Wang, S. G. Wang, A. Kohn, R. C. C. Ward, and A. K. Petford-Long, IEEE Trans. Magn. **43**, 2779 (2007).
[32] F. Shen, T. Zhu, X. Xiang, J. Q. Xiao, and Z. Zhang, J. Phys. D: Appl. Phys. **37**, 1515 (2004).
[33] D. J. Kim, J. Y. Bae, W. C. Lim, K. W. Kim, and T. D. Lee, J. Appl. Phys. **101**, 09B505 (2007).
[34] V. Serin, S. Andrieu, R. Serra, F. Bonell, C. Tiusan, L. Calmels, M. Varela, S. J. Pennycook, E. Snoeck, M. Walls, and C. Colliex, Phys. Rev. B **79**, 144413 (2009).
[35] J. J. Cha, J. C. Read, J. W. F. Egelhoff, P. Y. Huang, H. W. Tseng, Y. Li, R. A. Buhrman, and D. A. Muller, Appl. Phys. Lett. **95**, 032506 (2009).
[36] A. N. Chiaramonti, L. J. Thompson, W. F. Egelhoff, B. C. Kabius, and A. K. Petford-Long, Ultramicroscopy **108**, 1529 (2008).
[37] A. N. Chiaramonti, D. K. Schreiber, W. F. Egelhoff, D. N. Seidman, and A. K. Petford-Long, Appl. Phys. Lett. **93**, 103113 (2008).
[38] J. W. Lau, P. Morrow, J. C. Read, V. Hoink, W. F. Egelhoff, L. Huang, and Y. Zhu, Appl. Phys. Lett. **96**, 262508 (2010).
[39] L. A. Giannuzzi, B. W. Kempshall, S. M. Schwarz, J. K. Lomness, B. I. Prenitzer, and F. A. Stevie, in *Introduction to Focused Ion Beams*, edited by L. A. Giannuzzi and F. A. Stevie (Springer, New York, 2005), p. 201.
[40] W. F. Brinkman, R. C. Dynes, and J. M. Rowell, J. Appl. Phys. **41**, 1915 (1970).
[41] F. Hofer, P. Warbichler, and W. Grogger, Ultramicroscopy **59**, 15 (1995).
[42] E. Voelkl, L. Allard, and D. Joy, *Introduction to Electron Holography* (Plenum, New York, 1999).
[43] E. Volkl, L. F. Allard, and B. Frost, J. Microsc. Oxf. **180**, 39 (1995).
[44] D. D. Djayaprawira, K. Tsunekawa, M. Nagai, H. Maehara, S. Yamagata, N. Watanabe, S. Yuasa, Y. Suzuki, and K. Ando, Appl. Phys. Lett. **86**, 092502 (2005).
[45] T. Miyajima, T. Ibusuki, S. Umehara, M. Sato, S. Eguchi, M. Tsukada, and Y. Kataoka, Appl. Phys. Lett. **94**, 122501 (2009).
[46] X. Zhong, B. Kabius, D. Schreiber, J. Eastman, D. Fong, and A. Petford-Long, Microsc. Microanal. **15**, 600 (2009).
[47] K. Yamamoto, T. Hirayama, and T. Tanji, Ultramicroscopy **101**, 265 (2004).
[48] B. Kabius, P. Hartel, M. Haider, H. Müller, S. Uhlemann, U. Loebau, J. Zach, and H. Rose, J. Electron. Microsc. **58**, 147 (2009).
[49] G. H. Yu and X. Peng, Appl. Surf. Sci. **256**, 6592 (2010).
[50] P. Rottländer, M. Hehn, and A. Schuhl, Phys. Rev. B **65**, 054422 (2002).
[51] J. Schmalhorst, A. Thomas, G. Reiss, X. Kou, and E. Arenholz, J. Appl. Phys. **102**, 053907 (2007).
[52] A. T. Hindmarch, K. J. Dempsey, D. Ciudad, E. Negusse, D. A. Arena, and C. H. Marrows, Appl. Phys. Lett. **96**, 092501 (2010).
[53] J. Wingbermuhle, S. Stein, and H. Kohlstedt, J. Appl. Phys. **92**, 7261 (2002).
[54] J. C. A. Huang, C. Y. Hsu, W. H. Chen, and Y. H. Lee, IEEE Trans. Magn. **43**, 911 (2007).
[55] J. van Elp, J. L. Wieland, H. Eskes, P. Kuiper, G. A. Sawatzky, F. M. F. de Groot, and T. S. Turner, Phys. Rev. B **44**, 6090 (1991).
[56] V. I. Anisimov *et al.*, J. Phys. Condens. Matter **2**, 3973 (1990).
[57] B.-s. Kim, S. Hong, and D. W. Lynch, Phys. Rev. B **41**, 12227 (1990).
[58] R. L. Hengehold and F. L. Pedrotti, J. Appl. Phys. **47**, 287 (1976).
[59] Y. A. Valbis, K. A. Kalder, I. L. Kuusmann, Ch. B. Lushchik, A. A. Ratas, Z. A. Rachko, M. E. Springis, and V. M. Tift, JEPT. Lett. **22**, 36 (1975).
[60] W. G. Wang, C. Ni, A. Rumaiz, Y. Wang, X. Fan, T. Moriyama, R. Cao, Q. Y. Wen, H. W. Zhang, and J. Q. Xiao, Appl. Phys. Lett. **92**, 152501 (2008).

[61] G. Landry, X. Xiang, J. Du, and J. Q. Xiao, J. Magn. Magn. Mater. **226**, 920 (2001).

[62] F. Montaigne, M. Hehn, and A. Schuhl, Phys. Rev. B **64**, 144402 (2001)

[63] L. Le Brizoual, P. Alnot, M. Hehn, F. Montaigne, M. Alnot, A. Schuhl, and E. Snoeck, Appl. Phys. Lett. **86**, 112505 (2005).

[64] X. H. Xiang, T. Zhu, G. Landry, J. Du, Y. W. Zhao, and J. Q. Xiao, Appl. Phys. Lett. **83**, 2826 (2003).

[65] D. M. Newns, Phys. Rev. B **1**, 3304 (1970).

[66] J. A. Appelbaum and G. A. Baraff, Phys. Rev. B **4**, 1246 (1971).

[67] W. Wulfhekel, M. Klaua, D. Ullmann, F. Zavaliche, J. Kirschner, R. Urban, T. Monchesky, and B. Heinrich, Appl. Phys. Lett. **78**, 509 (2001).